

Palladium gates for reproducible quantum dots in silicon

Matthias Brauns^{1,*}, Sergey V. Amitonov¹, Paul-Christiaan Spruijtenburg¹, and Floris A. Zwanenburg¹

¹NanoElectronics Group, MESA+ Institute for Nanotechnology, University of Twente, P.O. Box 217, 7500 AE Enschede, The Netherlands

*matthias.brauns@ist.ac.at, present address: Institute of Science and Technology Austria, Am Campus 1, 3400 Klosterneuburg, Austria

ABSTRACT

We replace the established aluminium gates for the formation of quantum dots in silicon with gates made from palladium. We study the morphology of both aluminium and palladium gates with transmission electron microscopy. The native aluminium oxide is found to be formed all around the aluminium gates, which could lead to the formation of unintentional dots. Therefore, we report on a novel fabrication route that replaces aluminium and its native oxide by palladium with atomic-layer-deposition-grown aluminium oxide. Using this approach, we show the formation of low-disorder gate-defined quantum dots, which are reproducible across several fabrication runs. Furthermore, palladium enables us to further shrink the gate design, allowing us to perform electron transport measurements in the few-electron regime in devices comprising only two gate layers, a major technological advancement.

Introduction

The realization of a quantum computer using spins in a solid-state system^{1,2} has made impressive progress over the last decades. In recent years, group-IV materials like silicon³ and carbon⁴ have attracted a lot of attention, since they can be isotopically purified to only consist of spin-zero nuclei. Metal-oxide-semiconductor devices inspired by classical transistors have proven to be highly suitable for the realization of quantum bits both in intrinsic silicon and silicon-germanium heterostructures^{3,5}. Their very flexible design has enabled single and double quantum dots⁶⁻⁹, spin read-out via Pauli spin blockade¹⁰⁻¹⁵, charge sensing experiments with a quantum point contact¹⁶ and dispersive read-out¹⁷, single qubits^{10,18-21} and two-qubit logic gates²² in quick succession. With the realization of these building blocks, the first steps towards scaling-up have put the focus on the fabrication of reproducible, fully gate-tuneable devices.^{23,24} This remains challenging due to the formation of unintentional quantum dots.²⁵⁻²⁷

In this Report, we propose the use of an alternative gate metal, palladium, and compare its performance to the commonly used aluminium. In a first part, we characterize the suitability of the two materials as nanoscale gates by means of transmission electron microscopy (TEM). Subsequently, we assess the usability of devices fabricated with Pd gates for the formation of electrostatically defined quantum dots.

Transmission electron microscopy

The structures used for the TEM studies are displayed in Figure 1. The sample layout follows the pioneering device design of Angus et al.,⁶ the workhorse for the impressive follow-up experiments performed at the University of New South Wales.^{18,22,28-33} A quasi-intrinsic Si wafer is thermally oxidized to form approximately 8 nm of high-quality silicon oxide. In contrast to the original Angus design, we grow an additional dielectric layer of 5 nm aluminium oxide by atomic layer deposition (ALD). In the aluminium gate samples, this layer protects the SiO₂ from partially being reduced to SiO_x with $x < 2$. This reduction due to the stronger oxidation affinity of aluminium otherwise leads to defects directly underneath the gates. The gate structures are then formed by standard electron-beam lithography and lift-off. At least two layers of gates are required for quantum dot definition. Hence we thermally oxidize the aluminium samples to form a 5 nm layer of Al₂O₃ around the Al gates in Figure 1(a). Since palladium is a noble metal, this is not possible in these samples, and we therefore use ALD to achieve 5 nm of Al₂O₃ for the samples in Figure 1(b).

The gates in Figure 1 have a nominal width of 20-30 nm. This width is decreased in the case of Al due to the partial oxidation of the gates. Figure 1(a) reveals a very important feature of the commonly used Al gate structures: The oxidation process takes

place all around the gate, i.e. not only at the aluminium surface directly subjected to air, but also at the interface between the aluminium and the ALD-grown Al_2O_3 . Due to the incorporation of oxygen atoms, this necessarily leads to a volume increase at the bottom of the Al gate. The generated strain then leads to band structure modulations, and therefore the localization of charges at low temperatures, similarly to quantum dot formation due to different thermal expansion coefficients²⁷. Lim et al.⁸ observed a similar aluminium oxide formation at the Al-SiO₂ interface in their devices. Quantum dots formed below a single gate have been successfully used to demonstrate single-hole tunneling^{34,35} and electron quantum bits.¹⁸ For individual control over the electrochemical potential of the quantum dot as well as the tunnel barriers, however, these strain-induced quantum dots are detrimental.

The palladium gates in Figure 1(b) do not oxidize, avoiding above mentioned problems. The smaller grain size of the palladium thin films compared to the aluminium films grown in the same electron-beam evaporator also leads to overall more uniform gate structures. In conclusion, the TEM study suggests that gate structures similar to the Angus design made from palladium instead of aluminium can achieve more reproducibility in the formation of quantum dots with individual control over the tunnel barriers and dot potential by means of several gates.

Reproducible quantum dot devices

In Figure 2(a), a typical device used for studying the reproducibility of tuneable quantum dot devices is displayed. 25 nm wide barrier gates with a center-to-center distance of 60 nm are defined and covered by a 5 nm thick Al_2O_3 dielectric layer followed by a lead gate with a width of 30 nm between the barrier gates. An additional 5 nm Al_2O_3 is grown on top the whole gate structure before the devices are annealed for 30 min at 400°C in a hydrogen atmosphere. The quantum dot formed under the lead gate between the barrier gates thus has a size of approximately 35 by 30 nm.

In Figure 2(b) we show data of devices from three separate chips, i.e. apart from the SiO₂ and lowest Al_2O_3 layer, they have been fabricated in three separate fabrication runs in order to demonstrate chip-to-chip reproducibility. All measurements shown in Figure 2 have been performed at 4.2 K. A constant bias voltage of $V_{\text{SD}} = 1$ mV was applied to the ohmic contact overlapping with the lead gate left on the as indicated in the sketch in Figure 2(a), and the current flowing from the drain to ground was measured. The upper row in Figure 2(b) contains current versus gate voltage curves for all three devices. We will call the green curves in Figure 2(b), where the voltage is applied to the lead gate and both barrier gates simultaneously, turn-on curves. The measurements for the blue (orange) curves were performed by applying a constant voltage of 4 V to the lead gate and the right (left) barrier gate to ensure electron accumulation between them, and changing the voltage on the left (right) barrier from 4 V to 0 V. We will refer to them as pinch-off curves for the left (right) barrier gate.

While all devices turn on at voltages between 2 and 3 V, the pinch-off curves show a significantly lower and much steeper threshold voltage for pinching off the conductance channel, very much like Angus et al.⁶ observed. In all three devices the pinch-off curves exhibit only very few or even no resonance around the threshold voltage. Such resonances are commonly attributed to resonant tunneling via localized states within the created tunnel barrier, as discussed in the previous section.

An even clearer picture on the device physics can be drawn based on the data shown below the respective current vs. gate voltage curves. Here, the voltages on the barriers V_{b1} and V_{b2} are varied while a constant voltage $V_{\text{lead}} = 4$ V is applied to the lead gate. All three charge stability diagrams reveal diagonal lines, indicating the formation of a single quantum dot with equal capacitive coupling to both barriers. For Device A, only a single instability around $V_{b1} = 1780$ mV is visible. Device B also mainly exhibits one resonance below one of the barriers at $V_{b2} = 1320$ mV, which leads to deviations from the ideal single quantum dot picture indicating the formation of a strongly coupled double quantum dot of the quantum dot between the barriers with one unintentional one below barrier 2.³⁶ Finally, Device C is completely free of deviations from the ideal single quantum dot behaviour across many charge transitions, suggesting a defect-free electrostatic environment of the quantum dot.

In order to validate the findings from the barrier 1 versus barrier 2 plots, we measured two more devices from the same chip as Device A in a dilution refrigerator with an electron temperature of approximately 25 mK. In Figure 3(a) and (c) we plot charge stability diagrams, where we change V_{lead} versus V_{b1} and V_{b2} , with a fixed offset of $V_{b2} = V_{b1} + 300$ mV. Again, parallel, equally spaced current peaks indicate the formation of a single quantum dot. These Coulomb oscillations are only disturbed along two parallel lines marked by a red and a blue arrow in (a), and a single line marked by a red arrow in (c). These disturbances are most likely caused by a defect capacitively coupled to our quantum dot, varying the electrostatic environment by changing its own charge state. Since these two charging events follow parallel lines in gate space in Figure 3(a), they most likely have the same origin.

Bias spectroscopy measurements are displayed for both devices in Figures 3(b) and (d), where we plot the numerical differential conductance dI/dV_{SD} while changing V_{SD} and the gate voltages on all three gates simultaneously to follow the

dashed lines in Figures 3(a) and (c). In both cases, the measurements reveal Coulomb diamonds of constant height and shape, indicating a stable electrostatic environment and quantum dot shape and size. The charging energy is approximately 6 meV in both cases. The clean bias spectroscopy plots exhibit additional lines of increased conductance, which can be explained by, e.g., orbital excited states.^{37,38} In conclusion, our experiments show that by using palladium gates, electrostatic definition of quantum dots can be reproducibly achieved.

Few-electron quantum dots with two-layer devices

Reaching the few-electron regime in gate-defined quantum dots in silicon has proven to be very difficult due to the comparably high effective mass of the electrons³, a problem that has successfully been circumvented by employing a more complex gate stack with a third layer comprising a dedicated plunger gate.³⁹

Palladium as a gate metal provides us with an opportunity to reach the few-electron regime without complicating the device design: shrinking the size of the quantum dot to hold fewer electrons to start with. Since they do not oxidize, we can shrink the width of the barrier gates as well as their thickness to approximately 10-15 nm without risking broken gates due to oxidation. This allows us to scale down the barrier gate pitch to 40 nm (Figure 4(a)). The charge stability diagram in Figure 4(b), where we change V_{b1} and V_{b2} , displays again diagonal Coulomb oscillation, but far fewer than in the 60 nm pitch devices in Figure 3.

A further signature for the lower number of electrons on this quantum dot is revealed in Figure 4(c), where we plot I_{SD} versus V_{lead} and V_{b1} , with $V_{b2} = V_{b1} - 300$. The Coulomb peaks are parallel, signature for the formation of a single quantum dot, but not equidistant. The peak spacing ΔV_{b1} in Figure 4(d) shows a clear even-odd effect. This deviation from the constant interaction model⁴⁰ can be explained by the lower number of electrons on the quantum dot, where orbital effects start playing a role.⁴¹ The current is non-zero between Coulomb peaks for $V_{b1} \gtrsim 1550$ mV at $V_{lead} = 4000$ mV, a sign for the tunnel barriers being transparent enough for inelastic processes to become significant.³⁸ At lower barrier gate voltages, the Coulomb peaks are well-separated by Coulomb blockade, and at $V_{b1} < 1410$ mV for $V_{lead} = 3500$ mV, no Coulomb peak is visible any more. There are two possible explanations for this: Either the quantum dot is empty at this point, or the tunnel barriers simply have become too opaque to allow for a measurable Coulomb peak even though there are still electron states available.

Since our device does not feature a charge sensor¹⁶, we are restricted to transport measurements, which makes it difficult to distinguish the two scenarios. A signature of a not yet empty quantum dot is a saw-tooth-like pattern at finite bias³⁵, whereas a clean opening of the Coulomb diamond up to high source-drain bias voltages^{39,42-44} is a strong sign for the absence of available charge states, i.e. an empty quantum dot. Figure 4(e) shows a bias spectroscopy of the first two charge transitions visible in Figure 4(c). For barrier gate voltages lower than $V_{b1} = 1410$ mV, the onset of conductance opens up without any disturbance up to the measurement range of $V_{SD} = \pm 50$ mV, just as expected for an empty dot. Further evidence for reaching the single-electron regime is provided by the addition energies E_{add} of the first electrons added to the quantum dot: While $E_{add} = 17$ meV for the second electron entering the dot, the energy needed to add the third electron is significantly higher ($E_{add} = 24$ meV). This can be explained by a significant orbital energy E_{orb} leading to an even-odd effect for the charging energies.³⁸ $E_{orb} \approx 7$ meV is consistent with a line of increased conductance visible for positive V_{SD} in the first Coulomb diamond, which could thus represent the first orbital excited state.³⁷ The even-odd effect due to the additional orbital energy in Figures 4(d) and (e) becomes weaker for higher numbers of electrons, in accordance with findings in other systems.^{43,45-47}

The undisturbed high-bias opening of the last Coulomb diamond combined with the even-odd filling of the first electrons onto the quantum dot provides strong evidence for the observation of the single-electron regime in our device with the 40-nm gate pitch.

Conclusion

In conclusion, we have demonstrated the extraordinary suitability of palladium with ALD-grown aluminium oxide for gate stacks in MOSFET-like quantum dot devices in silicon. They provide excellent run-to-run reproducibility in fabrication, since chemical alterations of the silicon oxide layer below the gate are avoided, and additional stress due to an oxidation-related volume increase at the gate-dielectric interface does not occur. The small grain size and nobility of palladium also allow for device dimensions small enough to reach the few-electron regime even in two-layer gate designs, something very unusual in accumulation-mode devices in silicon. Performing transport measurements through quantum dots down to the last electron is highly desirable in fundamental research, since a direct energy scale is provided by the applied source-drain bias, which makes spectroscopy measurements much more feasible than by using charge sensing techniques. It also facilitates the read-out of single-spin quantum bits via Pauli spin blockade.

References

1. Loss, D. & DiVincenzo, D. P. Quantum computation with quantum dots. *Phys. Rev. A* **57**, 120–126 (1998). DOI 10.1103/PhysRevA.57.120.
2. Kane, B. E. A Silicon-Based Nuclear Spin Quantum Computer. *Nat.* **393**, 133–137 (1998). DOI 10.1038/30156.
3. Zwanenburg, F. A. *et al.* Silicon quantum electronics. *Rev. Mod. Phys.* **85**, 961–1019 (2013). DOI 10.1103/RevModPhys.85.961.
4. Laird, E. A. *et al.* Quantum transport in carbon nanotubes. *Rev. Mod. Phys.* **87**, 703–764 (2015). DOI 10.1103/RevModPhys.87.703.
5. Morton, J. J. L., McCamey, D. R., Eriksson, M. A. & Lyon, S. A. Embracing the quantum limit in silicon computing. *Nat.* **479**, 345–353 (2011). DOI 10.1038/nature10681.
6. Angus, S. J., Ferguson, A. J., Dzurak, A. S. & Clark, R. G. Gate-defined quantum dots in intrinsic silicon. *Nano letters* **7**, 2051–5 (2007). DOI 10.1021/nl070949k.
7. Simmons, C. B. *et al.* Charge sensing and controllable tunnel coupling in a Si/SiGe double quantum dot. *Nano letters* **9**, 3234–8 (2009). DOI 10.1021/nl9014974.
8. Lim, W. H. *et al.* Electrostatically defined few-electron double quantum dot in silicon. *Appl. Phys. Lett.* **94**, 173502 (2009). DOI 10.1063/1.3124242.
9. Tracy, L. a. *et al.* Double quantum dot with tunable coupling in an enhancement-mode silicon metal-oxide semiconductor device with lateral geometry. *Appl. Phys. Lett.* **97**, 192110 (2010). DOI 10.1063/1.3518058.
10. Maune, B. M. *et al.* Coherent singlet-triplet oscillations in a silicon-based double quantum dot. *Nat.* **481**, 344–347 (2012). DOI 10.1038/nature10707.
11. Liu, H. *et al.* Pauli-spin-blockade transport through a silicon double quantum dot. *Phys. Rev. B* **77**, 073310 (2008). DOI 10.1103/PhysRevB.77.073310.
12. Lai, N. S. *et al.* Pauli spin blockade in a highly tunable silicon double quantum dot. *Sci. reports* **1**, 110 (2011). DOI 10.1038/srep00110.
13. Li, R., Hudson, F. E., Dzurak, A. S. & Hamilton, A. R. Pauli Spin Blockade of Heavy Holes in a Silicon Double Quantum Dot. Supporting Information. *Nano Lett.* **15**, 7314–7318 (2015). DOI 10.1021/acs.nanolett.5b02561.
14. Betz, A. C. *et al.* Dispersively Detected Pauli Spin-Blockade in a Silicon Nanowire Field-Effect Transistor. *Nano Lett.* **15**, 4622–4627 (2015). DOI 10.1021/acs.nanolett.5b01306.
15. Borselli, M. G. *et al.* Pauli spin blockade in undoped Si/SiGe two-electron double quantum dots. *Appl. Phys. Lett.* **99**, 1–4 (2011). DOI 10.1063/1.3623479.
16. Simmons, C. B. *et al.* Single-electron quantum dot in Si/SiGe with integrated charge sensing. *Appl. Phys. Lett.* **91**, 213103 (2007). DOI 10.1063/1.2816331.
17. Gonzalez-Zalba, M. F. *et al.* Gate-Sensing Coherent Charge Oscillations in a Silicon Field-Effect Transistor. *Nano Lett.* **16**, 1614–1619 (2016). DOI 10.1021/acs.nanolett.5b04356.
18. Veldhorst, M. *et al.* An addressable quantum dot qubit with fault-tolerant control-fidelity. *Nat. Nanotechnol.* **9**, 981–985 (2014).
19. Kim, D. *et al.* Quantum control and process tomography of a semiconductor quantum dot hybrid qubit. *Nat.* **1**, 1–12 (2014). DOI 10.1038/nature13407.
20. Maurand, R. *et al.* A CMOS silicon spin qubit. *Nat. Commun.* **7**, 13575 (2016).
21. Takeda, K. *et al.* A fault-tolerant addressable spin qubit in a natural silicon quantum dot. *Sci. Adv.* **2**, e1600694 (2016). DOI 10.1017/CBO9781107415324.004.
22. Veldhorst, M. *et al.* A two-qubit logic gate in silicon. *Nat.* **526**, 410–414 (2015). DOI 10.1038/nature15263.
23. Zajac, D. M., Hazard, T. M., Mi, X., Nielsen, E. & Petta, J. R. Scalable Gate Architecture for a One-Dimensional Array of Semiconductor Spin Qubits. *Phys. Rev. Appl.* **6**, 1–8 (2016). DOI 10.1103/PhysRevApplied.6.054013.
24. Spruijtenburg, P. C., Amitonov, S. V., Mueller, F., van der Wiel, W. G. & Zwanenburg, F. A. Passivation and characterization of charge defects in ambipolar silicon quantum dots. *Sci. Reports* **6**, 38127 (2016). DOI 10.1038/srep38127.
25. Ishikuro, H. & Hiramoto, T. On the origin of tunneling barriers in silicon single electron and single hole transistors. *Appl. Phys. Lett.* **74**, 1126–1128 (1999). DOI 10.1063/1.123464.

26. Mueller, F., Konstantaras, G., Van Der Wiel, W. G. & Zwanenburg, F. A. Single-charge transport in ambipolar silicon nanoscale field-effect transistors. *Appl. Phys. Lett.* **106**, 10–15 (2015). DOI 10.1063/1.4919110.
27. Thorbeck, T. & Zimmerman, N. M. Formation of strain-induced quantum dots in gated semiconductor nanostructures. *AIP Adv.* **5**, 087107 (2015). DOI 10.1063/1.4928320.
28. Morello, A. *et al.* Single-shot readout of an electron spin in silicon. *Nat.* **467**, 687–691 (2010). DOI 10.1038/nature09392.
29. Pla, J. J. *et al.* A single-atom electron spin qubit in silicon. *Nat.* **489**, 541–5 (2012). DOI 10.1038/nature11449.
30. Pla, J. J. *et al.* High-fidelity readout and control of a nuclear spin qubit in silicon. *Nat.* **496**, 334–338 (2013). DOI 10.1038/nature12011.
31. Laucht, A. *et al.* High-fidelity adiabatic inversion of a ³¹P electron spin qubit in natural silicon. *Appl. Phys. Lett.* **104**, 092115 (2014). DOI 10.1063/1.4867905.
32. Muhonen, J. T. *et al.* Storing quantum information for 30 seconds in a nanoelectronic device. *Nat. Nanotechnol.* **9**, 986–991 (2014). DOI 10.1038/nnano.2014.211.
33. Laucht, A. *et al.* Electrically controlling single-spin qubits in a continuous microwave field. *Sci.* 1–5 (2015).
34. Spruijtenburg, P. C. *et al.* Single-hole tunneling through a two-dimensional hole gas in intrinsic silicon. *Appl. Phys. Lett.* **102**, 192105 (2013). DOI 10.1063/1.4804555.
35. Li, R., Hudson, F. E., Dzurak, A. S. & Hamilton, A. R. Single hole transport in a silicon metal-oxide-semiconductor quantum dot. *Appl. Phys. Lett.* **103**, 1–5 (2013). DOI 10.1063/1.4826183.
36. van der Wiel, W. G. *et al.* Electron transport through double quantum dots. *Rev. Mod. Phys.* **75**, 1–22 (2003). DOI 10.1103/RevModPhys.75.1.
37. Escott, C. C., Zwanenburg, F. A. & Morello, A. Resonant tunnelling features in quantum dots. *Nanotechnol.* **21**, 274018 (2010). DOI 10.1088/0957-4484/21/27/274018.
38. Hanson, R., Petta, J. R., Tarucha, S. & Vandersypen, L. M. K. Spins in few-electron quantum dots. *Rev. Mod. Phys.* **79**, 1217–1265 (2007). DOI 10.1103/RevModPhys.79.1217.
39. Lim, W. H. *et al.* Observation of the single-electron regime in a highly tunable silicon quantum dot. *Appl. Phys. Lett.* **95**, 242102 (2009). DOI 10.1063/1.3272858.
40. Kouwenhoven, L. P. *et al.* Electron transport in quantum dots. In *Proceedings of the NATO Advanced Study Institute on Mesoscopic Electron Transport*, 105–214 (1997).
41. Kouwenhoven, L. P., Austing, D. G. & Tarucha, S. Few-electron quantum dots. *Reports on Prog. Phys.* **64**, 701–736 (2001). DOI 10.1088/0034-4885/64/6/201.
42. Kouwenhoven, L. P. *et al.* Excitation spectra of circular, few-electron quantum dots. *Sci.* **278**, 1788–92 (1997). DOI 10.1126/science.278.5344.1788.
43. Jarillo-Herrero, P., Sapmaz, S., Dekker, C., Kouwenhoven, L. P. & Van Der Zant, H. S. J. Electron-hole symmetry in a semiconducting carbon nanotube quantum dot. *Nat.* **429**, 389–392 (2004). DOI 10.1038/nature02568.
44. Zwanenburg, F. A., van Rijmenam, C. E. W. M., Fang, Y., Lieber, C. M. & Kouwenhoven, L. P. Spin states of the first four holes in a silicon nanowire quantum dot. *Nano letters* **9**, 1071–9 (2009). DOI 10.1021/nl803440s.
45. Tarucha, S., Austing, D. G., Honda, T., van der Hage, R. J. & Kouwenhoven, L. P. Shell Filling and Spin Effects in a Few Electron Quantum Dot. *Phys. Rev. Lett.* **77**, 3613–3616 (1996).
46. Johnson, A. C., Petta, J. R., Marcus, C. M., Hanson, M. P. & Gossard, A. C. Singlet-triplet spin blockade and charge sensing in a few-electron double quantum dot. *Phys. Rev. B* **72**, 165308 (2005). DOI 10.1103/PhysRevB.72.165308.
47. Nilsson, H. A. *et al.* Giant, Level-dependent g factors in InSb nanowire quantum dots. *Nano Lett.* **9**, 3151–3156 (2009). DOI 10.1021/nl901333a.

Acknowledgements

The authors want to thank Joost Ridderbos and Wilfred van der Wiel for fruitful discussions. Tess Meijerink was so kind as to be of excellent support during the electron transport measurements. All authors want to express their gratitude to Hans Mertens and Rico Keim for technical support. This work is part of the research programme “Atomic physics in the solid state” with project number 14167, which is (partly) financed by the Netherlands Organisation for Scientific Research (NWO).

Author contributions statement

MB, SVA, and PCS fabricated the devices. MB and PCS performed the measurements. MB, PCS, and FAZ analysed the results. MB wrote the manuscript. All authors reviewed the manuscript.

Additional information

Competing financial interests The authors declare no competing financial interests.

Data availability statement The datasets generated during and/or analysed during the current study are available from the corresponding author on reasonable request.

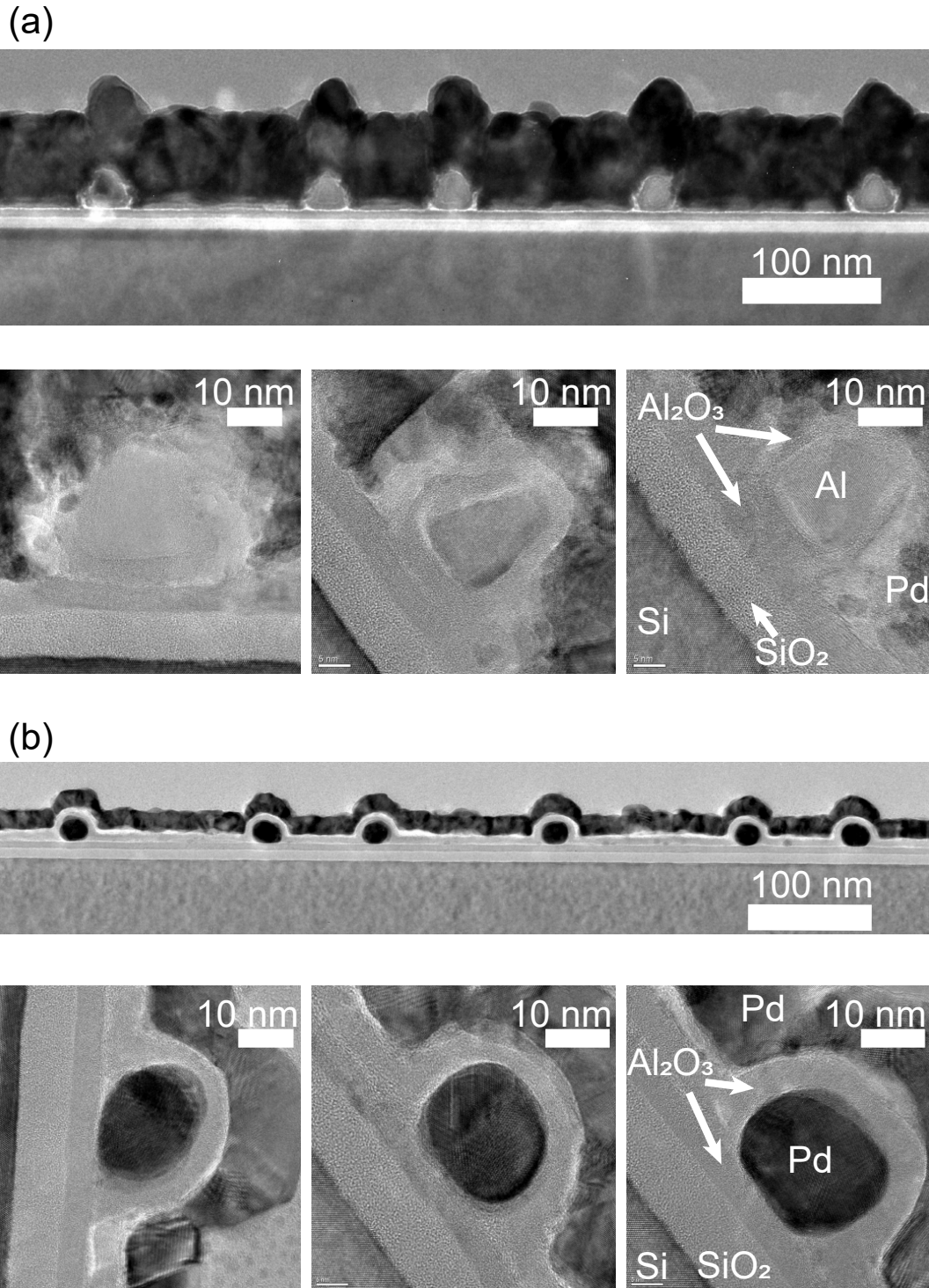


Figure 1. Transmission electron microscopy cross sections of (a) aluminium and (b) palladium gates on top of a Si-SiO₂-Al₂O₃ layer stack capped by Al₂O₃ and palladium.

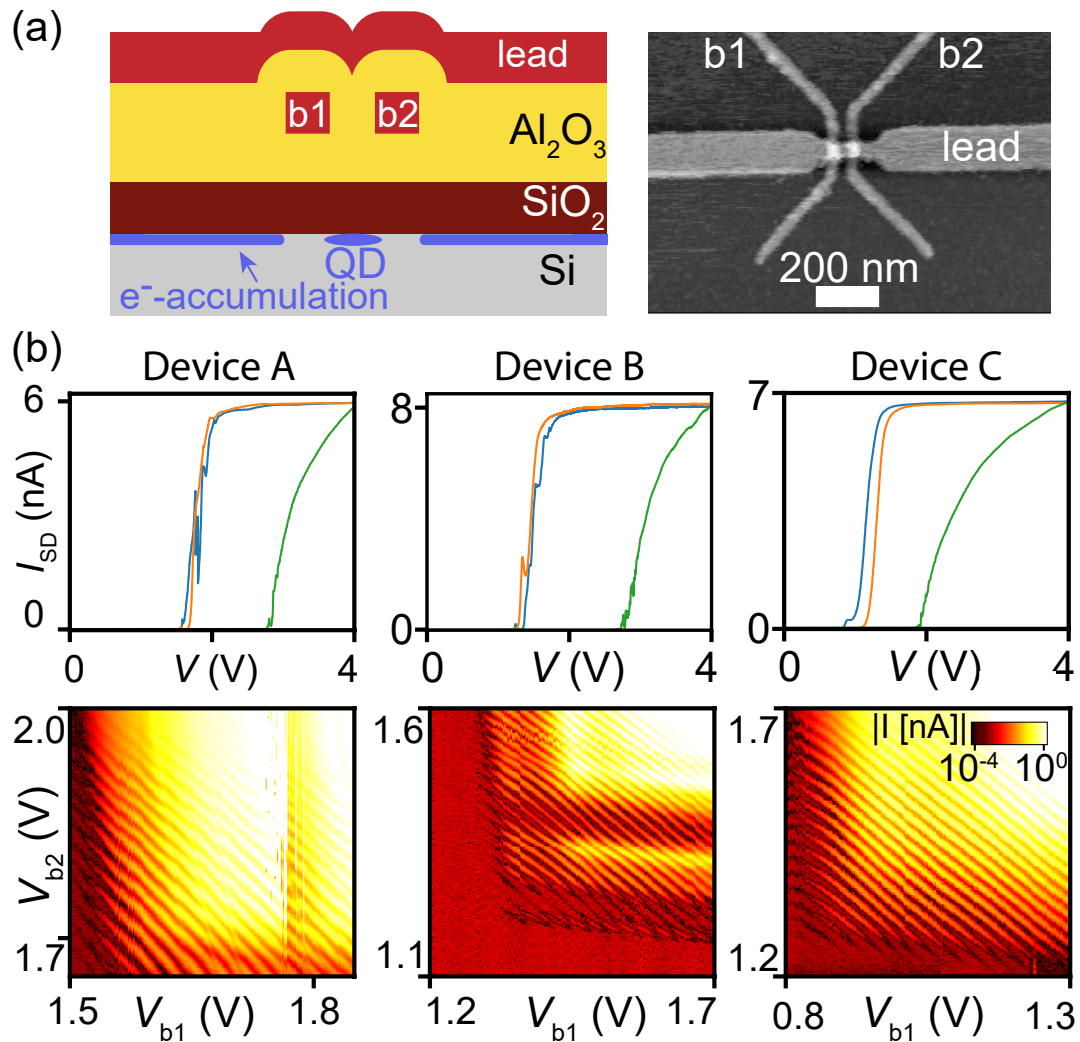


Figure 2. (a) Schematic cross-section and atomic-force microscopy top-view of a typical device. (b) Measurements taken at 4 K for three devices on three different chips. Top row: current vs gate voltage applied to all three gates simultaneously (green curve), and applied to barrier gate b1 (b2) [blue (orange) curve] while keeping the voltage on the other two gates at 4 V. Lower panel: current versus voltages on b1 and b2 with $V_{lead} = 4$ V.

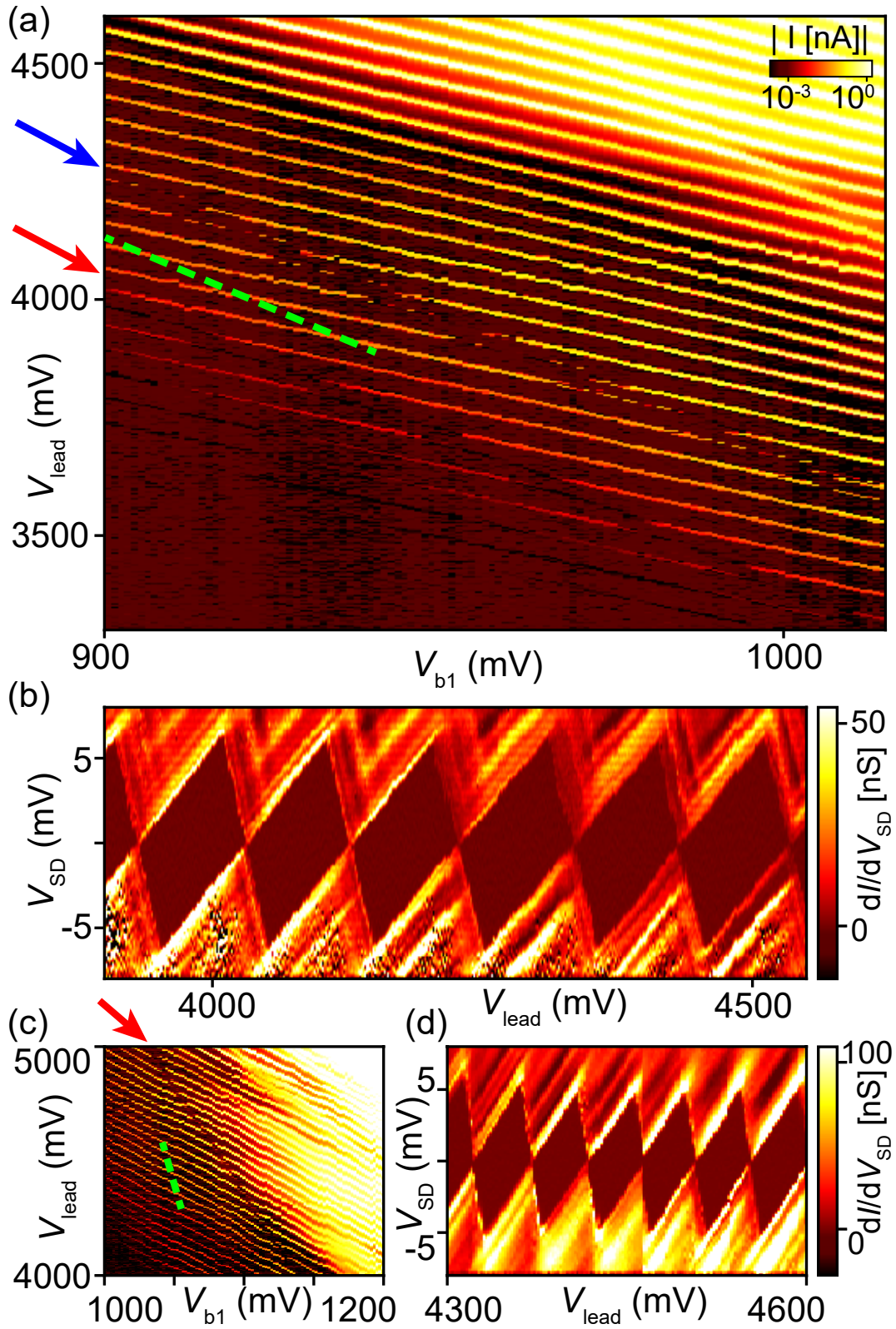


Figure 3. (a) and (c) current versus voltage on the lead gate and the barrier gate at $V_{SD} = 1$ mV. In (a), V_{b1} and V_{b2} are linked by $V_{b2} = V_{b1} + 300$ mV. In (c), $V_{b2} = V_{b1} - 250$ mV, and the colour scale is the same as in (a). The arrows indicate deviations from the single quantum dot picture. (b) and (d) are bias spectroscopy plots along the dashed lines in (a) and (c), respectively. All measurement performed at 25 mK.

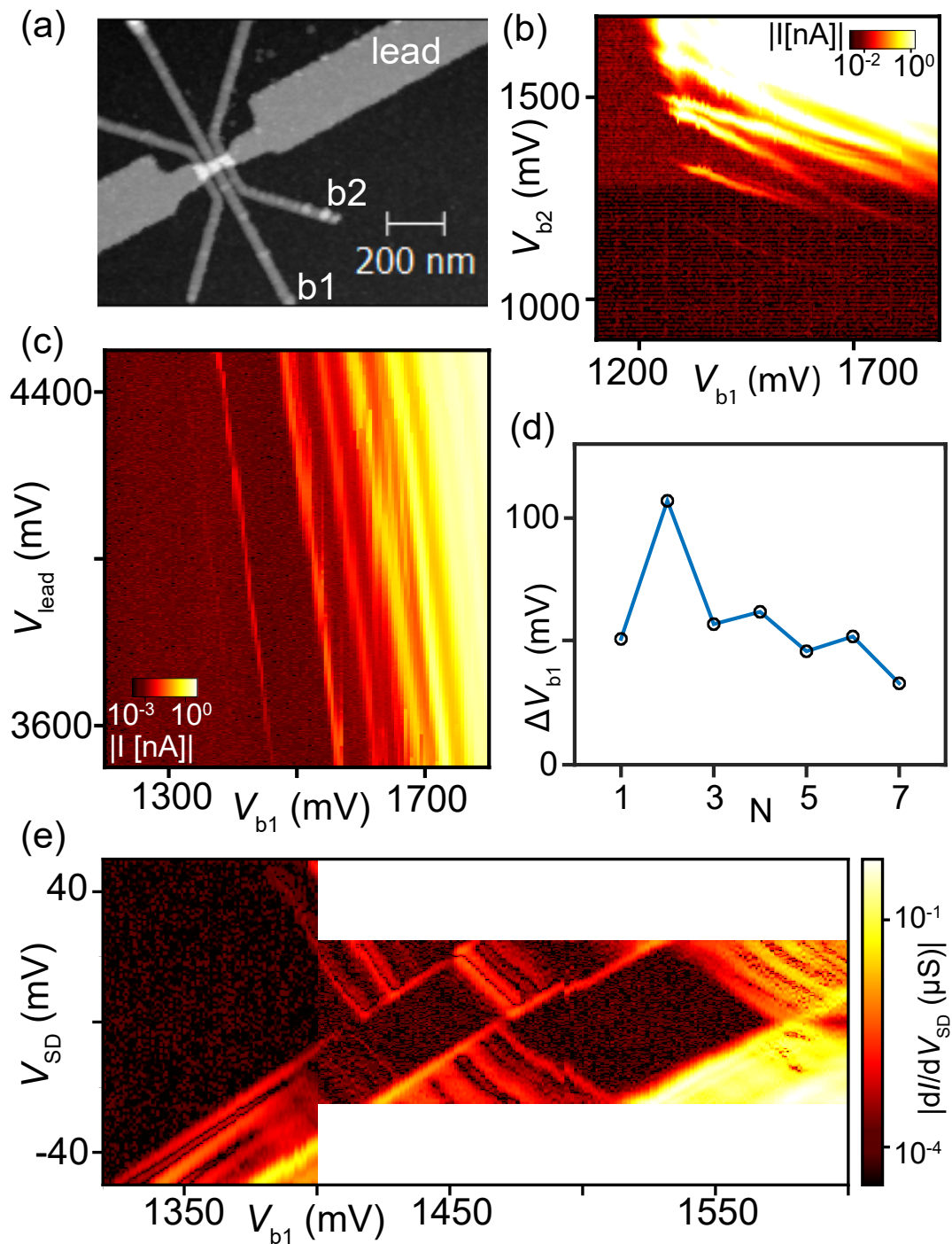


Figure 4. (a) AFM image of the device with a gate pitch of 40 nm. The leftmost barrier gate was not connected. (b) plot of I versus the voltages on the barrier gates b1 and b2 with fixed $V_{lead} = 4000$ mV. (c) I plotted versus $V_{lead} = 4000$ mV and $V_{b1} = V_{b2} + 300$ mV. (d) The Coulomb peak distance ΔV_{b1} between adjacent Coulomb peaks at $V_{lead} = 3500$ mV. (e) Differential conductance dI/dV_{SD} versus at $V_{lead} = 3500$ mV.